AGU PUBLICATIONS

JGR

Journal of Geophysical Research: Space Physics

RESEARCH ARTICLE
10.1002/2016JA023516

Special Section:
Major Results From the MAVEN Mission to Mars

Statistical analysis of the reflection of incident O^+ pickup ions at Mars: MAVEN observations

K. Masunaga[1], K. Seki[1], D. A. Brain[2], X. Fang[2], Y. Dong[2], B. M. Jakosky[2], J. P. McFadden[3], J. S. Halekas[4], J. E. P. Connerney[5], D. L. Mitchell[3], and F. G. Eparvier[2]

[1]Department of Earth and Planetary Science, Graduate School of Science, University of Tokyo, Tokyo, Japan, [2]Laboratory for Atmospheric and Space Physics, University of Colorado Boulder, Boulder, Colorado, USA, [3]Space Science Laboratory, University of California, Berkeley, California, USA, [4]Department of Physics and Astronomy, University of Iowa, Iowa City, Iowa, USA, [5]NASA Goddard Space Flight Center, Greenbelt, Maryland, USA

Abstract Analyzing ~1.3 year data set of O^+ ion velocity distribution functions obtained from the Suprathermal and Thermal Ion Composition instrument on the Mars Atmosphere and Volatile Evolution (MAVEN) spacecraft, we statistically investigate reflections of incident O^+ pickup ions (>10 keV) occurring below the Martian bow shock. To quantitatively evaluate importance of the reflection of incident O^+ pickup ions, we estimate reflection ratios by calculating average inward and outward O^+ ion fluxes above the Martian bow shock. Our result shows that an average reflection ratio is 14.1 ± 6.7%. We also investigate dependences of the reflection ratio on the solar wind, solar EUV flux, and southern hemispheric crustal magnetic field on Mars. We find that the reflection ratio strongly depends on the magnitude of the interplanetary magnetic field (IMF), solar wind dynamic pressure, and gyroradius of O^+ pickup ions in the solar wind, rather than the solar EUV flux and the crustal magnetic field. We suggest that the reflection ratio is determined by the magnetic field both in the solar wind and below the bow shock that mainly controls gyroradius of incident O^+ pickup ions in these regions. We also find that the reflection ratio increases to 38.9 ± 10.2% as these parameters become extreme conditions (i.e., IMF magnitude >6 nT). Since incident O^+ pickup ions are known to be a major source of atmospheric sputtering escape from Mars, our result suggests that ion reflections may have a role to reduce the sputtering escape from Mars under the extreme solar wind condition.

Key Points:
- Average reflection ratio of incident O^+ pickup ions from the Martian magnetosheath/magnetic pileup region is ~14%
- The reflection ratio reaches ~39% under extreme solar wind conditions
- The reflection ratio is determined by magnetic fields both in the solar wind and below the bow shock

Supporting Information:
- Supporting Information S1

Correspondence to:
K. Masunaga,
masu-kei@eps.s.u-tokyo.ac.jp

Citation:
Masunaga, K., et al. (2017), Statistical analysis of the reflection of incident O^+ pickup ions at Mars: MAVEN observations, *J. Geophys. Res. Space Physics*, *122*, doi:10.1002/2016JA023516.

Received 25 SEP 2016
Accepted 11 MAR 2017
Accepted article online 15 MAR 2017

1. Introduction

Due to the lack of an intrinsic magnetic field of Mars, the upper atmosphere of Mars directly interacts with the solar wind. Once neutral particles in the Martian corona are ionized by solar UV radiations, charge exchange, or electron impacts of the solar wind, they are accelerated by the convection electric field of the solar wind. This process is referred to as the ion pickup, and the ions are called pickup ions [e.g., *Coates and Jones*, 2009].

The ion pickup involves planetary ions into the solar wind, which slows down the solar wind. A bow shock forms at which the solar wind turns supersonic to subsonic speeds. Then the interplanetary magnetic field (IMF) starts to drape and piles up in front of the ionosphere. This forms the magnetic pileup region (MPR), where the magnetic field magnitude largely increases on the ionosphere, and a small-scale magnetosphere called the induced magnetosphere [*Luhmann et al.*, 2004].

The ion pickup is known to be one of the important ion escape processes at Mars. Around Mars, H^+ pickup ions are identified by the Phobos-2 [*Barabash and Lundin*, 1993], Mars Express [*Dubinin et al.*, 2006], and Mars Atmosphere and Volatile Evolution (MAVEN) spacecraft [*Rahmati et al.*, 2017]. These spacecraft also identified O^+ pickup ions around Mars [*Cravens et al.*, 2002; *Hara et al.*, 2013; *Rahmati et al.*, 2015]. Due to large gyroradius of O^+ pickup ions compared to the scale of the Marian size, the O^+ pickup ions escape Mars by forming a plume in the hemisphere in which the convection electric field points away from the planet (+E hemisphere) [*Fang et al.*, 2008; *Dong et al.*, 2015] but reenter into the Martian ionosphere in the hemisphere in which the electric field points to the planet (−E hemisphere) [*Fang et al.*, 2013; *Hara et al.*, 2013]. The incident O^+ ions are known to be an important source for sputtering, which drives atmospheric heating and escape at Mars [e.g., *Luhmann and Kozyra*, 1991; *Luhmann et al.*, 1992; *Leblanc and Johnson*, 2001; *Fang et al.*, 2013; *Wang et al.*, 2014, 2015]. *Luhmann et al.* [1992] suggested that the atmospheric sputtering played an important role in the atmospheric escape from Mars in the past, when the young Sun is thought to be more active [*Lammer et al.*, 2003].

Recently, *Masunaga et al*. [2016] identified that some of the incident O^+ pickup ions are reflected in the dayside magnetosheath due to strong electromagnetic fields in this region by analyzing the ion velocity distribution functions (VDFs) observed by the Suprathermal and Thermal Ion Composition (STATIC) instrument on MAVEN. The reflected O^+ ions become energetic O^+ ion beams (~10 keV or higher) in the solar wind with a narrow angular spread (typically, one or two angular bins of STATIC corresponding to 22.5–45°). Near the subsolar region, the beams tend to flow nearly in the sunward direction. In high solar zenith angle (SZA) regions such as SZA > 50°, the beams tend to flow nearly in the direction of the convection electric field in the + E hemisphere but in the opposite direction in the −E hemisphere. Since the incident O^+ pickup ions are a major source of sputtering with the Martian upper atmosphere, it is important to quantitatively evaluate the reflection of the incident O^+ pickup ions. In this paper, we statistically estimate what percent of incident O^+ pickup ions can be reflected to understand importance of the ion reflection by calculating inward and outward O^+ ion fluxes above the Martian bow shock. We also study its dependences on the solar wind, the solar EUV flux, and the position of the southern crustal magnetic field because the Martian plasma environment is highly affected by these parameters [*Brain et al*., 2005; *Ramstad et al*., 2015].

2. Instrumentations and Data Analysis Method

In this study, we analyze O^+ ion VDFs observed by the STATIC instrument aboard MAVEN during periods between November 2014 and February 2016. We use the data product of "d0" whose time resolution is 128 s in this period. We also use the Solar Wind Ion Analyzer, the Solar Wind Electron Analyzer, and the magnetometer to obtain proton density, velocity and temperatures, electron temperatures, and IMF vectors. To see the solar EUV flux at Mars, we use the Solar EUV Monitor as well. Details of each instrument are described in *McFadden et al*. [2015], *Halekas et al*. [2015], *Mitchell et al*. [2016], *Connerney et al*. [2015], and *Eparvier et al*. [2015], respectively.

Figures 1a–1c show a MAVEN position in the solar wind in the Mars Solar Electric (MSE) coordinate system (the *x* axis points to the Sun, the *z* axis points to the convection electric field, and the *y* axis completes the right-hand system) and an example of the O^+ ion VDF observed at this position. Figure 1d is an original O^+ ion VDF projected on the plane perpendicular to the local magnetic field (ion velocities within a range of ±45° from the perpendicular plane). We can see that two characteristic ion velocity distributions appear in this VDF. The first characteristic distribution is the ring distribution on the red dashed circle calculated by local proton velocity and magnetic field. This indicates that O^+ pickup ions drift to the $\mathbf{E_{SW}} \times \mathbf{B_{SW}}$ direction around the spacecraft. The center of the ring indicates the drift velocity of the guiding center which corresponds to the perpendicular solar wind velocity to the local magnetic field. The second characteristic distribution is O^+ ion beams with energy of ~10 keV flowing nearly toward the Sun. These beams are produced as incident O^+ pickup ions are reflected in the magnetosheath and return to the solar wind [*Masunaga et al*., 2016].

To quantitatively evaluate the reflection of incident O^+ pickup ions, we estimate a reflection ratio of incident O^+ pickup ions. To do this, we statistically map outward and inward O^+ fluxes through the bow shock. We divide the ion VDF into two parts in terms of the shock normal direction: parallel directed (outward) and antiparallel directed (inward) parts to the shock normal vector. The two parts are identified from the red dash-dotted line indicating the shock tangent perpendicular to the shock normal vector as shown in Figure 1d. Note that the shock normal vector is defined per 5° (latitude) × 5° (clock angle) area binned on the empirical dayside bow shock of *Edberg et al*. [2008] and then we find the nearest shock normal vector connecting to one of these bins based on the MAVEN position.

Then we calculate outward and inward O^+ ion fluxes through the bow shock. However, as shown in Figure 1d, we observed O^+ pickup ions on the ring distribution in the VDF as well as reflected O^+ beams. The early velocity phase of the ring distribution corresponds to the "ion plume" accelerated toward the convection electric field direction in the +E hemisphere [*Dong et al*., 2015]. The plume contains O^+ ions picked up in the solar wind and those originated below the bow shock. These ions are neither reflected from nor entering into the Martian magnetosheath. Thus, we need to remove them from each ion VDF to calculate correct outward and inward fluxes above the bow shock to estimate the reflection ratio.

Figures 1e and 1f show outward and inward directed O^+ ion VDFs to the shock surface, respectively. The area surrounded by the yellow curves indicates the initial quarter part of the velocity phase of the ring distribution

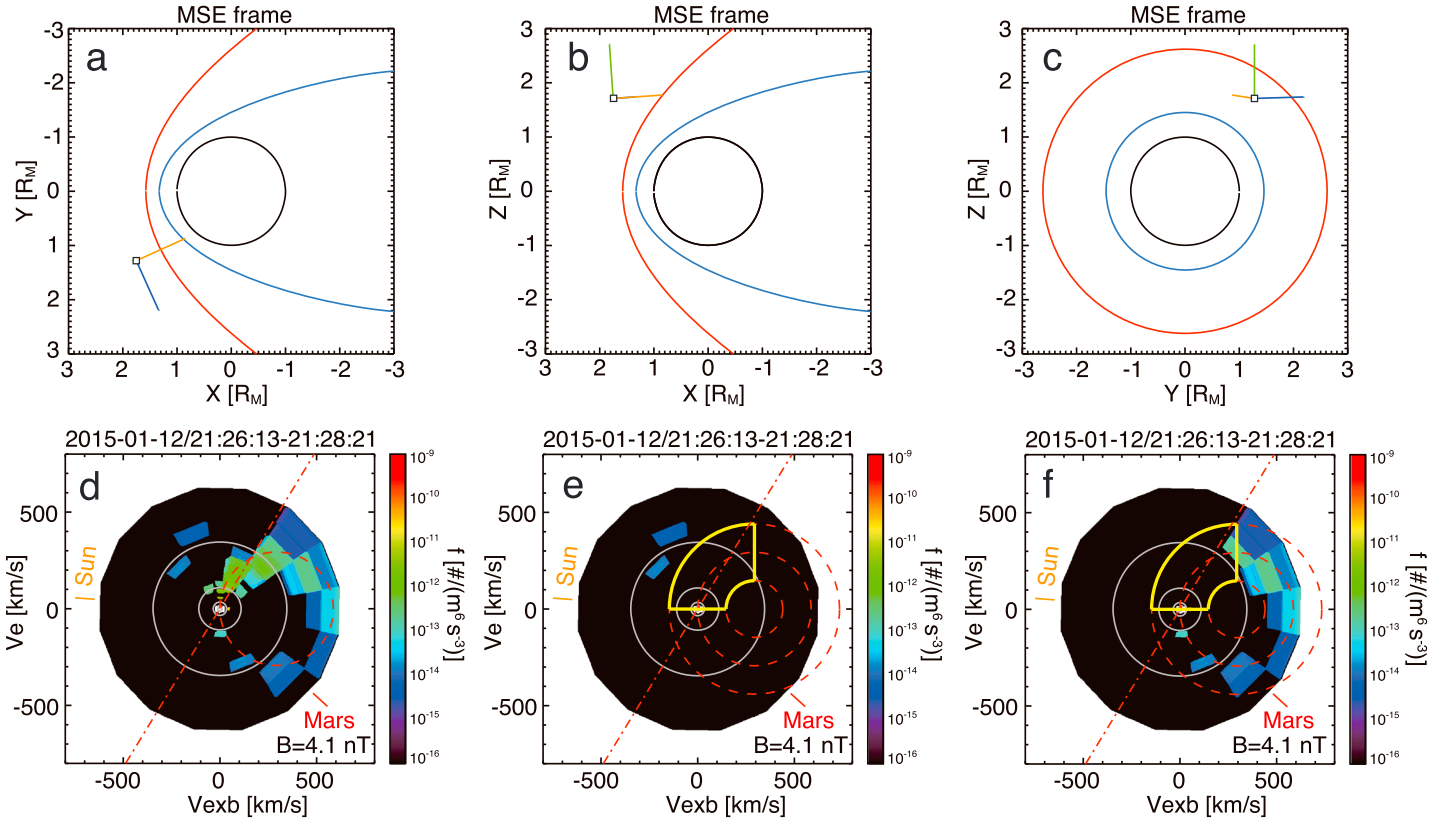

Figure 1. (a–c) MAVEN position is shown by a small black square in the MSE coordinate system. The black circle is the Martian disk. The red and blue curves correspond to empirical bow shock and magnetic pileup boundary, respectively [*Edberg et al.*, 2008]. The local IMF, local proton velocity (perpendicular to the local IMF), and local convection electric field directions are shown by blue, orange, and green lines on the MAVEN position, respectively. (d) O^+ ion VDF projected on the plane perpendicular to the local magnetic field (within ±45° from the perpendicular plane) observed by STATIC. Gray circles indicate 100 eV, 1 keV, and 10 keV contours, respectively. The red dashed circle indicates an ideal ring distribution calculated by local proton velocity and magnetic field. The red dash-dotted line indicates a shock surface tangent. The red and orange lines indicate Mars and Sun directions, respectively. (e, f) Outward and inward directed O^+ ion VDFs toward the shock surface, respectively. The yellow part in these VDFs corresponds to the first quarter velocity phase of the ring distribution with a ±50% velocity width which corresponds to inner and outer red dashed rings in these figures. All ion distributions inside the yellow part are removed from the VDF.

with ±50% velocity width. This width is chosen based on our sensitive analysis of the velocity width shown in the supporting information. We assume that ions in this area are not reflected from or entering into the Martian magnetosheath as explained above. Thus, we removed all ions in this area from each VDF and then calculate correct outward and inward fluxes. Note that although this ring distribution may not hold in the magnetosheath, this method properly removes plume ions accelerated from the magnetosheath as well as those in the solar wind (see supporting information). Since the ion plume is mainly observed in the +E hemisphere, we have applied this method only when MAVEN is in the +E hemisphere.

3. Observations

Using 86,729 VDFs, we calculated the outward and inward O^+ fluxes above the Martian bow shock. Figure 2 shows average outgoing and incoming O^+ fluxes (>10 keV) and number of measurements projected on the dayside bow shock in the MSE frame. Note that the bins that have less than three samples are discarded for better statistics. The fluxes in Figures 2a and 2b are calculated from original VDFs (the original case). For the outgoing ions of this case, we can see that strong outgoing ion fluxes appear in the +E hemisphere in Figure 2a. The strong fluxes correspond to the O^+ ion plume mainly originating from the ionosphere, the magnetosheath, or the exosphere above the bow shock in the +E hemisphere [e.g., *Fang et al.*, 2008]. For the incoming ions in Figure 2b, we can see a strong inward O^+ ion fluxes in the −E hemisphere because denser O^+ ions precipitate toward Mars in the −E hemisphere. This feature is consistent with previous studies [*Luhmann and Kozyra*, 1991; *Hara et al.*, 2013]. The fluxes in Figures 2c and 2d are calculated by applying the plume removal

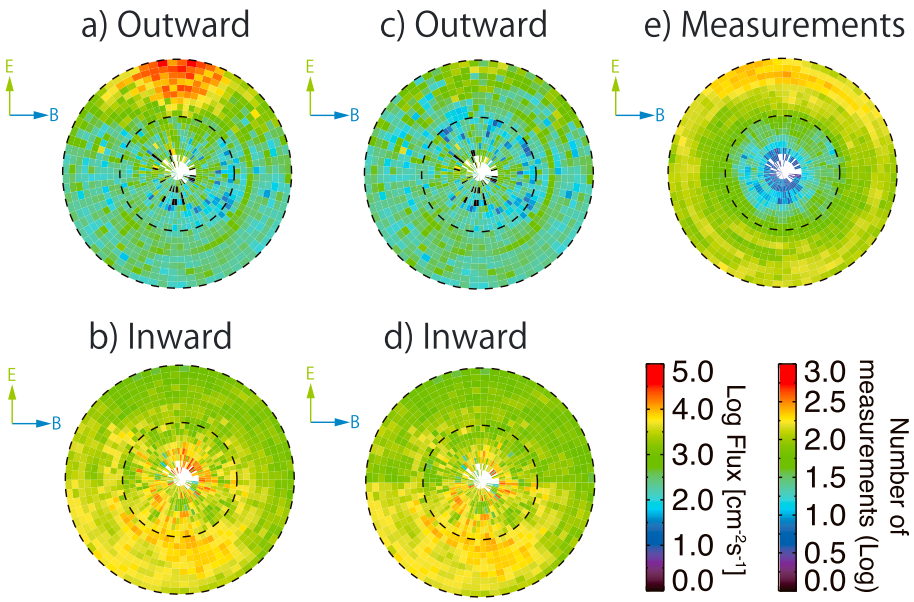

Figure 2. Outward and inward O^+ ion fluxes projected on the dayside Martian bow shock in the MSE frame using (a and b) original O^+ ion VDFs and (c and d) plume removed VDFs. Radial and azimuth directions indicate the solar zenith angle (SZA) and the IMF clock angle, respectively. So the center of the map indicates the subsolar point, and black dashed circles are 45° and 90° SZAs, respectively. (e) The number of measurements in each bin. The white bins in each map indicate discarded bins in which measurements are less than three samples.

method explained in section 2 (the plume removal case). For the outgoing ions of this case, we can see that the strong fluxes in the +E hemisphere seen in the original case mostly disappear as seen in Figure 2c. For the incoming ions, the plume removing method results in inward O^+ fluxes in the +E hemisphere slightly reduced from the original case as seen in Figure 2d.

Table 1 shows the average O^+ ion outgoing and incoming rates from the dayside bow shock (Q_{out} and Q_{in}) and their ratio (R). These values and errors are calculated as follows:

$$Q = \sum_i A_i f_i, \quad \Delta Q = \sqrt{\sum_i (A_i \Delta f_i)^2}, \tag{1}$$

$$R = \frac{Q_{out}}{Q_{in}}, \quad \Delta R = \sqrt{\left(\frac{\Delta Q_{out}}{Q_{in}}\right)^2 + \left(\frac{Q_{out}}{Q_{in}^2} \cdot \Delta Q_{in}\right)^2}, \tag{2}$$

where A_i, f_i, and Δf_i are an area, average outward/inward fluxes, and their standard deviation of the ith bin. We can see that there is a large difference of the ion outgoing rate but slight difference of the ion incoming rate between the original and plume removal cases. The ion outgoing rate calculated from the plume removal case is $(1.26 \pm 0.59) \times 10^{21}\ s^{-1}$ that is much smaller than the original case ($(6.10 \pm 3.10) \times 10^{21}\ s^{-1}$). The ion incoming rate calculated from the plume removal case is $(8.97 \pm 0.66) \times 10^{21}\ s^{-1}$ that is slightly smaller than the original case ($(9.88 \pm 0.70) \times 10^{21}\ s^{-1}$). As a result, we estimate the reflection ratio for the plume removal case of $14.1 \pm 6.7\%$.

Table 1. Outgoing and Incoming Rates of O^+ Ions Through the Bow Shock and Their Ratio Calculated by Using Original O^+ Ion VDFs and "Plume Removed" VDFs[a]

	Original	Removed
Outward	(6.10 ± 3.10)E + 21	(1.26 ± 0.59)E + 21
Inward	(9.88 ± 0.70)E + 21	(8.97 ± 0.66)E + 21
Ratio	61.8 ± 31.7%	14.1 ± 6.7%

[a]Unit of ion outgoing/incoming rates is s^{-1}.

We also investigate dependences of the reflection ratio on the solar wind. Figure 3 shows histograms

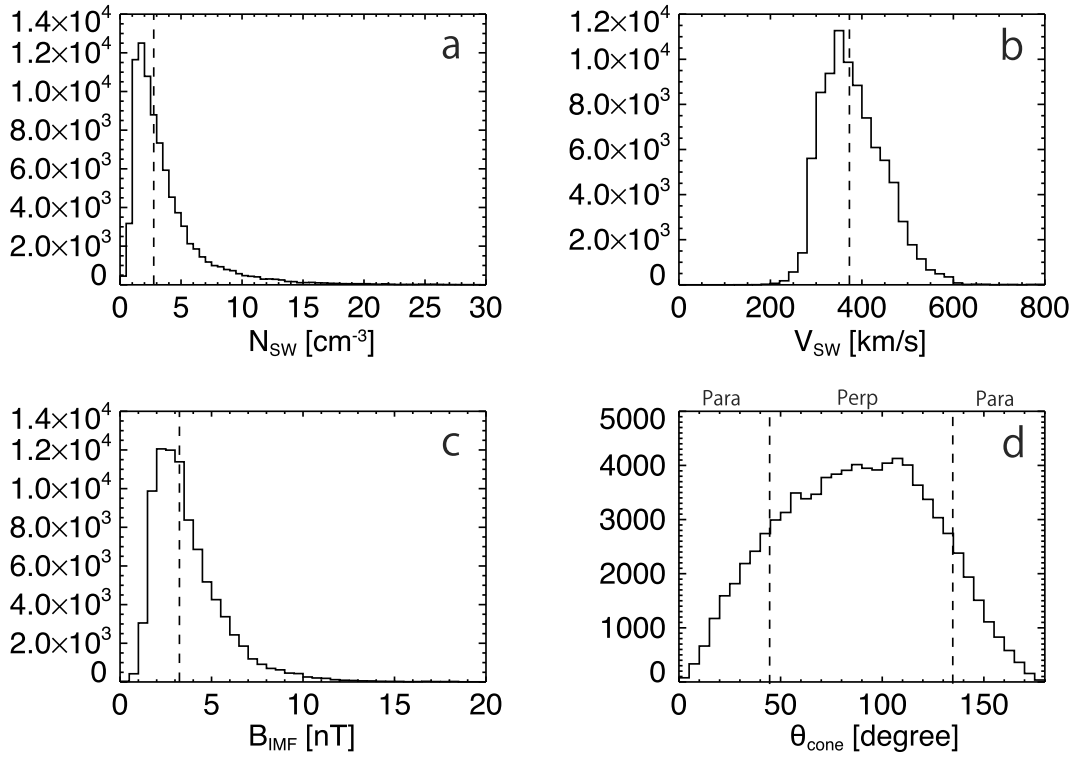

Figure 3. Histograms of solar wind conditions: (a) proton density, (b) proton velocity, (c) IMF magnitude, and (d) IMF cone angle. For the Figures 3a–3c, the vertical dashed lines indicate a median value of each parameter. For Figure 3d, the vertical dashed lines indicate criterion of $\theta_{cone} = 45°$ and 135° that sort data set into the perpendicular or parallel IMF case.

for four solar wind parameters taken into account: proton density (N_{SW}), proton velocity (V_{SW}), IMF magnitude (B_{IMF}), and IMF cone angle (θ_{cone}). The vertical dotted line in Figures 3a–3c shows the median value of each parameter. To see which parameters likely to contribute to the ion reflection ratio, the outward and inward flux maps shown in Figures 2c and 2d are sorted into two cases depending on whether these parameters are smaller or larger than their median value. For the IMF cone angle (Figure 3d), the maps are sorted into the two cases: perpendicular IMF case ($45° \leq \theta_{cone} \leq 135°$) or the parallel IMF case ($\theta_{cone} < 45°$ or $\theta_{cone} > 135°$).

Figure 4 shows outward and inward O^+ ion flux maps sorted by the four solar wind conditions. The O^+ ion outgoing/incoming rates and its reflection ratios are also shown in this figure. Figure 4a is the flux maps for small and large N_{SW} cases. We can clearly see that both outgoing and incoming fluxes become large for the large N_{SW} case than those for the small N_{SW} case. The reflection ratio is 17.9 ± 7.0% for the large N_{SW} case, which is significantly larger than that of the small N_{SW} case (6.5 ± 2.8%). We also see clear dependences of the outgoing and incoming fluxes on B_{IMF} (Figure 4c). Similar to N_{SW} cases, both outgoing and incoming fluxes increase as B_{IMF} increases. The reflection ratio becomes significantly larger for the large B_{IMF} case than that for the small B_{IMF} case (18.0 ± 6.6% versus 5.9 ± 4.3%). On the other hand, we do not see clear dependences of the outgoing and incoming fluxes on V_{SW} (Figure 4b). Both outgoing/incoming fluxes look similar between the small and large V_{SW} cases. The reflection ratio is not significantly different between the large V_{SW} case (19.1 ± 9.7%) and the small V_{SW} case (10.2 ± 3.9%). Regarding the IMF cone angle, inward fluxes are clearly different between the perpendicular and parallel IMF cases (Figure 4d). Outward fluxes look similar between the two cases, but some strong flux spots appear for the parallel IMF case. The reflection ratio is very large (29.1 ± 14.4%) for the parallel IMF case, but it is also moderate level for the perpendicular IMF case (10.9 ± 4.6%). Due to the large errors, the reflection ratio is not significantly different between the two IMF cone angles.

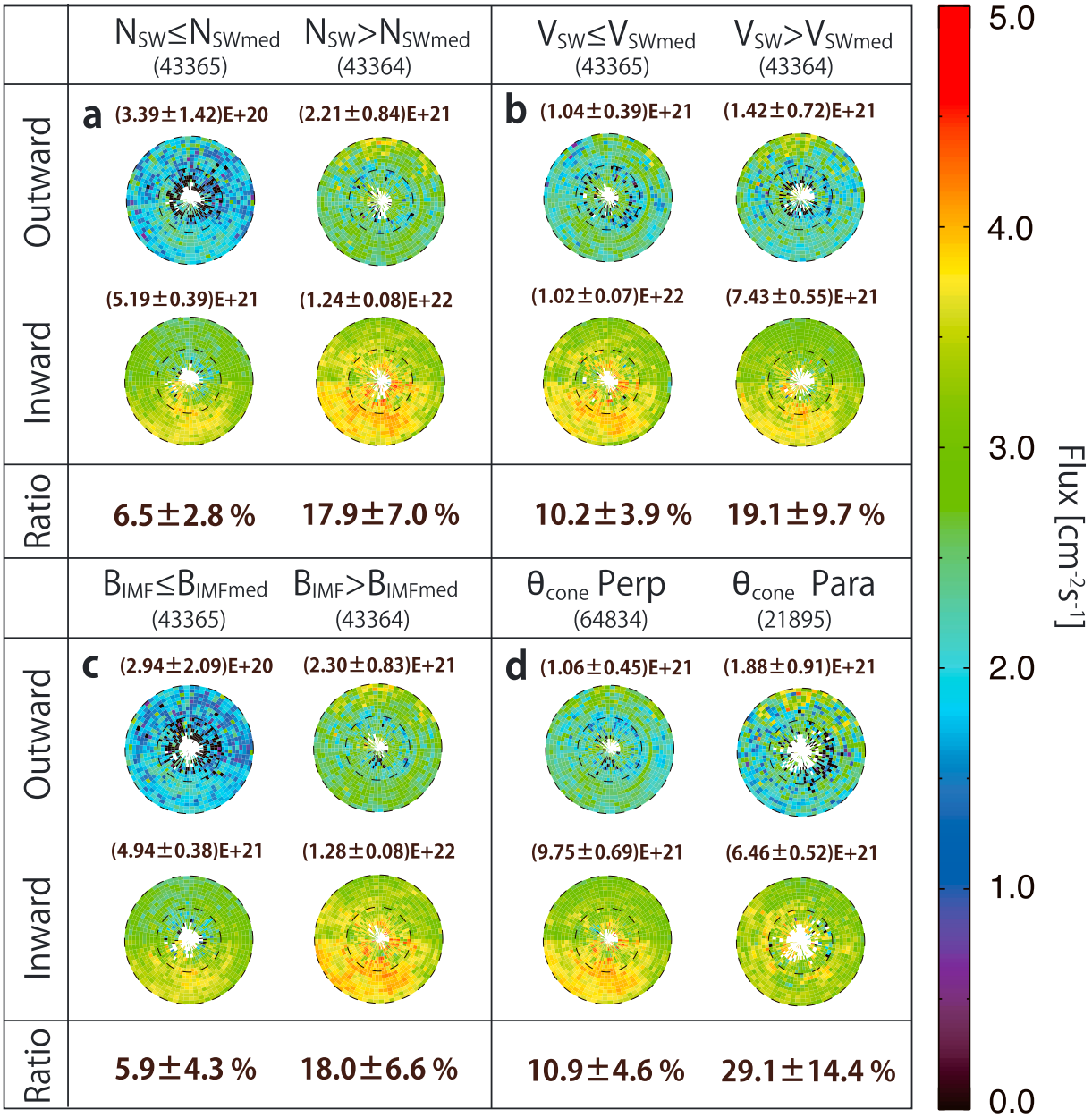

Figure 4. Outward and inward O^+ ion fluxes through the dayside bow shock in the MSE frame for different solar wind conditions: (a) proton density, (b) proton velocity, (c) IMF magnitude, and (d) cone angle. Numbers shown below each solar wind condition indicate the number of VDFs used to calculate fluxes. Each number shown above these flux maps indicates ion outgoing/incoming rates (s^{-1}). Each reflection ratio is calculated from the outgoing rate divided by the incoming rate.

We further investigate the effects of the solar wind parameters composed of a few fundamental solar wind parameters: the dynamic pressure (P_{dyn}), gyroradius of O^+ pickup ions in the solar wind (R_{O+}), and the magnetosonic Mach number (M_{MS}), which are calculated as follows:

$$P_{dyn} = m_p N_{SW} V_{SW}^2, \tag{3}$$

$$R_{O^+} = \frac{m_O V_{SWperp}}{eB_{IMF}}, \tag{4}$$

$$M_{MS} = \frac{V_{SW}}{\sqrt{V_A^2 + V_S^2}}, \tag{5}$$

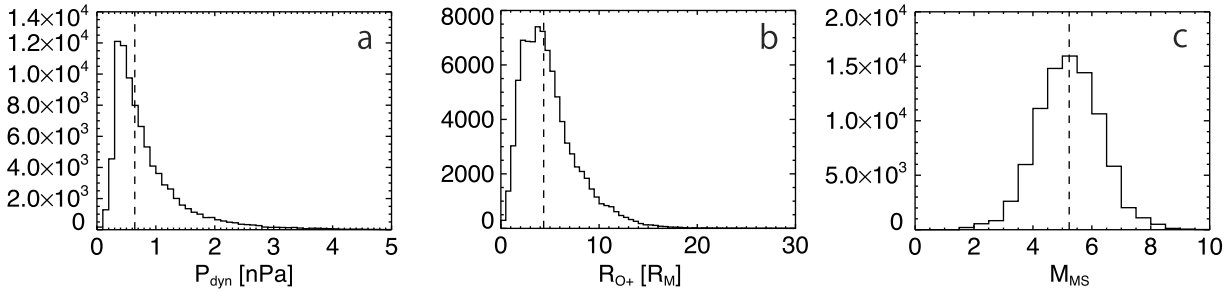

Figure 5. Histograms of solar wind conditions: (a) the solar wind dynamic pressure, (b) gyroradius of O^+ pickup ions in the solar wind, and (c) the magnetosonic Mach number. The vertical dashed lines indicate a median value of each parameter.

where m_p, m_o, V_{SWperp}, and e indicate mass of proton and oxygen ions, the solar wind velocity perpendicular to IMF, and the elementary charge, respectively. V_A and V_S indicate the Alfvén speed and the sound speed, respectively:

$$V_A = \frac{B_{IMF}}{\sqrt{\mu_0 m_p N_{SW}}}, \tag{6}$$

$$V_S = \sqrt{\frac{\gamma k_B (T_e + T_i)}{m_p}}, \tag{7}$$

where μ_0, γ, k_B, T_e, and T_i indicate the permeability of vacuum, the ratio of specific heats, Bolzmann's constant, and electron and ion temperatures, respectively. Figure 5 shows histograms of P_{dyn}, R_{O+}, and M_{MS} in the same format as Figure 3. Figure 6 shows the outward/inward ion fluxes sorted by their median parameters in the same format as Figure 4. In each parameter, we can see clear dependences in the outward/inward fluxes. Both outward and inward fluxes become large for the large P_{dyn}, small R_{O+} and small M_{MS} cases. We can see significant differences in the reflection ratios between the two P_{dyn} cases (5.3 ± 1.3% for the small P_{dyn} case and 18.2 ± 7.0% for the large P_{dyn} case) and between the two R_{O+} cases (19.5 ± 7.3% for the small R_{O+} case and 5.1 ± 3.0% for the large R_{O+} case). On the other hand, we do not see a significant difference in the reflection ratio between the small and large M_{MS} cases (17.2 ± 6.6% for the small M_{MS} case and 9.9 ± 6.5% for the large M_{MS} case).

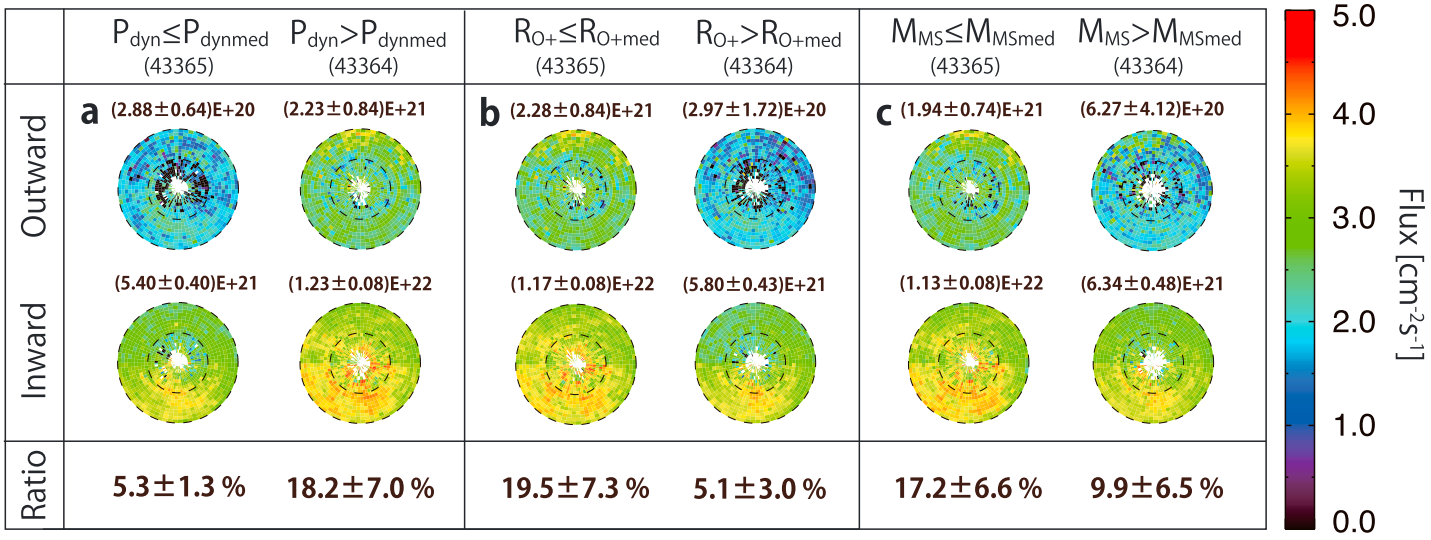

Figure 6. Outward and inward O^+ ion fluxes through the dayside bow shock in the MSE frame for different solar wind conditions: (a) dynamic pressure, (b) gyroradius of O^+ pickup ions in the solar wind, and (c) the magnetosonic Mach number. The format is the same as Figure 4.

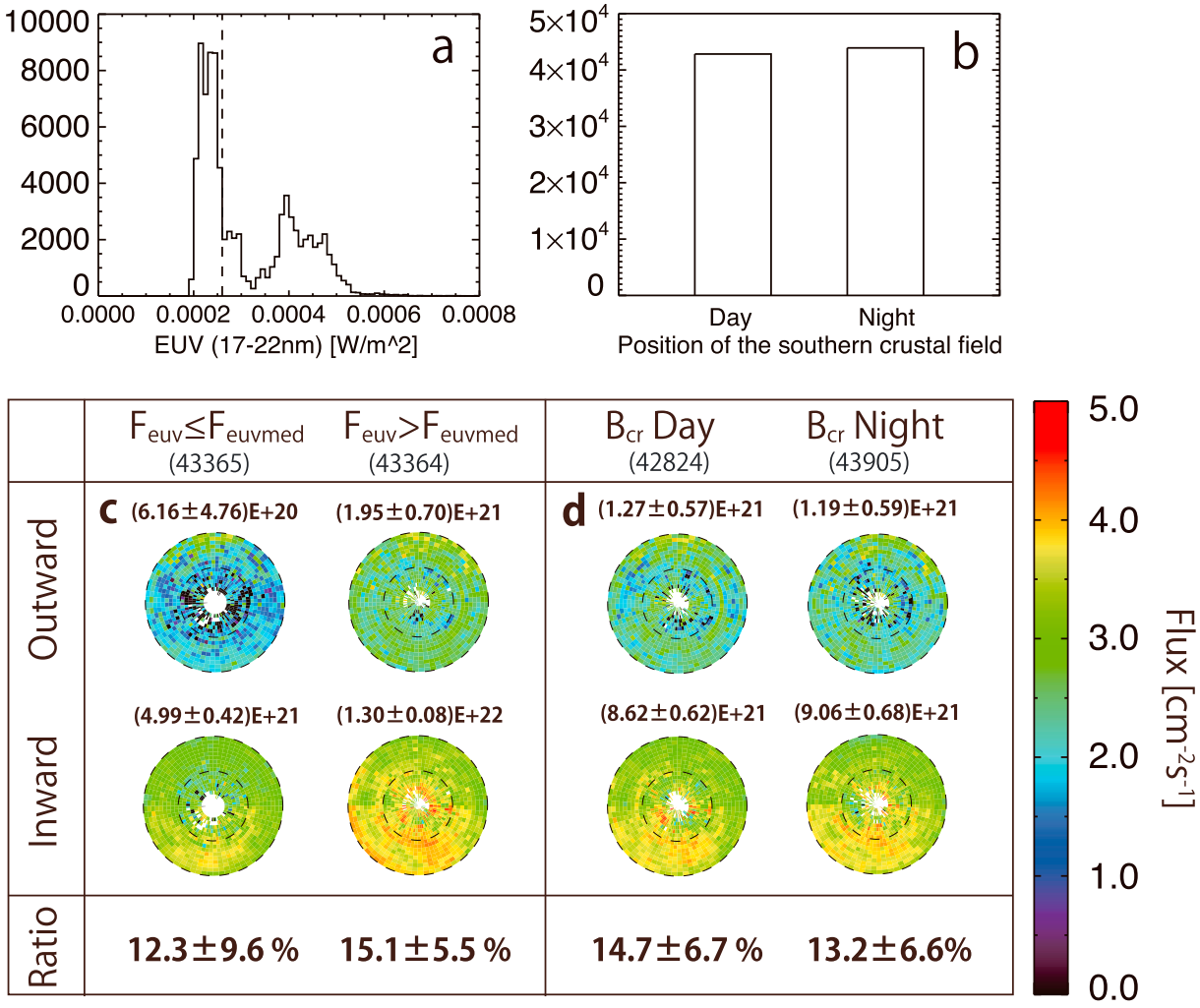

Figure 7. (a and b) Histogram for the solar EUV flux and the position of the southern crustal magnetic field. The vertical dashed line in Figure 7a indicates a median value of the EUV flux. (c and d) Outward and inward O^+ ion fluxes for the different EUV flux and different position of the crustal magnetic field. The format is the same as Figure 4.

We also examine the effects of the solar EUV flux (F_{EUV}) and the crustal magnetic field (B_{cr}) in the southern hemisphere (53°S and 179°E) on the reflection ratio. Note that to see the crustal magnetic field effects, the flux maps are divided into two cases according to whether the southern crustal magnetic field locates on the dayside or nightside. Figure 7 shows their histogram as well as their inward/outward fluxes and ratios. In Figure 7c, we can see that outward/inward fluxes increase as the EUV flux increases. However, the reflection ratio is not significantly different between the small F_{EUV} case and the large F_{EUV} case (12.3 ± 9.6% for the small F_{EUV} case and 15.1 ± 5.5% for the large F_{EUV} case). In Figure 7d, both outward and inward fluxes look similar between the two B_{cr} cases. The reflection ratio is also similar between the two B_{cr} cases (14.7 ± 6.7% for the dayside B_{cr} case and 13.2 ± 6.6% for the nightside B_{cr} case).

4. Discussion

We statistically investigated outward and inward O^+ ion fluxes (>10 keV) above the Martian bow shock and estimated an average reflection ratio of the incident O^+ pickup ions. Using ~1.3 year data set of O^+ ion VDFs, we obtained the average reflection ratio of 14.1 ± 6.7%. We also investigated their dependences on the solar wind, the solar EUV flux, and the southern hemispheric crustal magnetic field of Mars. It was found that the fluxes and the reflection ratio showed significant dependences on some of the solar wind

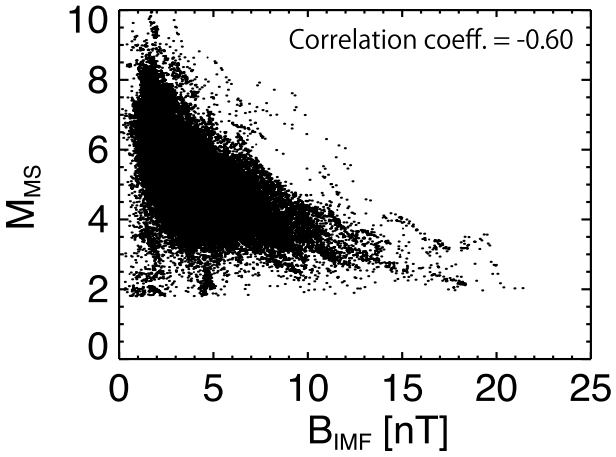

Figure 8. Scatterplot of the IMF magnitude and the magnetosonic Mach number.

conditions. The solar EUV flux did not significantly change the reflection ratio, although it affected the outward/inward fluxes. The position of the southern crustal magnetic field did not affect the outward/inward fluxes and the reflection ratio. Among the solar wind parameters, the reflection ratio was strongly affected by the IMF magnitude, dynamic pressure, and gyroradius of O^+ pickup ions in the solar wind. Note that the significant dependences of the reflection ratio on the dynamic pressure and the gyroradius are mainly due to changes of proton density and IMF magnitude, respectively, since the solar wind velocity does not strongly affect the reflection ratio (see Figure 4b). When the IMF magnitude and dynamic pressure become large, the reflection ratio increases. On the other hand, it increases when the O^+ gyroradius becomes small. This suggests that magnetic fields both in the solar wind and below the bow shock play a role to determine the reflection ratio by controlling gyroradius of incident O^+ pickup ions in these regions.

In the solar wind, the IMF magnitude mainly controls the gyroradius of the O^+ pickup ions. When the IMF magnitude is large, the gyroradius of O^+ pickup ions become small and thus dense pickup ions close to Mars have more chances to reenter the magnetosheath. This results in increasing inward fluxes, which may result in increasing the outward fluxes as well (see Figure 4c).

Below the bow shock, gyroradius of incident O^+ pickup ions is initially controlled by the magnetic field in the magnetosheath. The sheath magnetic field is usually larger than the upstream IMF magnitude due to the shock jump across the bow shock. The large sheath magnetic field makes the gyroradius of incident O^+ pickup ions even smaller. When the gyroradius is enough small compared to the scale of the magnetosehath, some of the incident O^+ pickup ions can gyrate in the magnetosheath and flick back to the solar wind, which may increase the reflection ratio.

The shock jump rate depends on the magnetosonic Mach number. It corresponds to ~2–3 when the Mach number ranges ~2–6 according to past Venus observations [*Tatrallyay et al*., 1984]. Since the Mach number ranges ~2–10 in our observation (see Figure 5c), the shock jump rate is also ~2–3 by applying the result of *Tatrallyay et al*. [1984].

Figure 8 shows a scatterplot of the IMF magnitude and the magnetosonic Mach number. We can see that the IMF magnitude varies between ~0.2 and 20 nT and there is a negative correlation between the IMF magnitude and the Mach number. Due to the large variation of the IMF magnitude and to the fact that the shock jump rate is at most ~3, we can see that the shock jump effect is less important than the upstream IMF magnitude to form a large magnetic field in the magnetosheath. This means that the shock jump effect of the magnetic field across the shock is overwhelmed by variations of the upstream IMF magnitude, leading to the inverse dependence of the reflection ratio on the Mach number as shown in Figure 6c. Thus, we suggest that the O^+ reflection in the magnetosheath is mainly controlled by the upstream IMF magnitude.

Some of incident O^+ pickup ions further go down to MPR. In MPR, the solar wind dynamic pressure balances with the magnetic pressure [*Crider et al*., 2003]. From the pressure balance equation ($P_{dyn} = P_{MPR} = {B_{MPR}}^2/2\,\mu_0$ where P_{MPR} and B_{MPR} represent the magnetic pressure and the magnitude of the magnetic field in MPR, respectively), we can see that the solar wind dynamic pressure is a proxy for the magnitude of the magnetic field in MPR. Thus, a large dynamic pressure indicates that a large magnetic field exists in MPR. This means that the gyroradius of the incident O^+ pickup ions become small in MPR under the large dynamic pressure. As similar to the case of the magnetosheath, more incident O^+ pickup ions can gyrate in MPR and flick

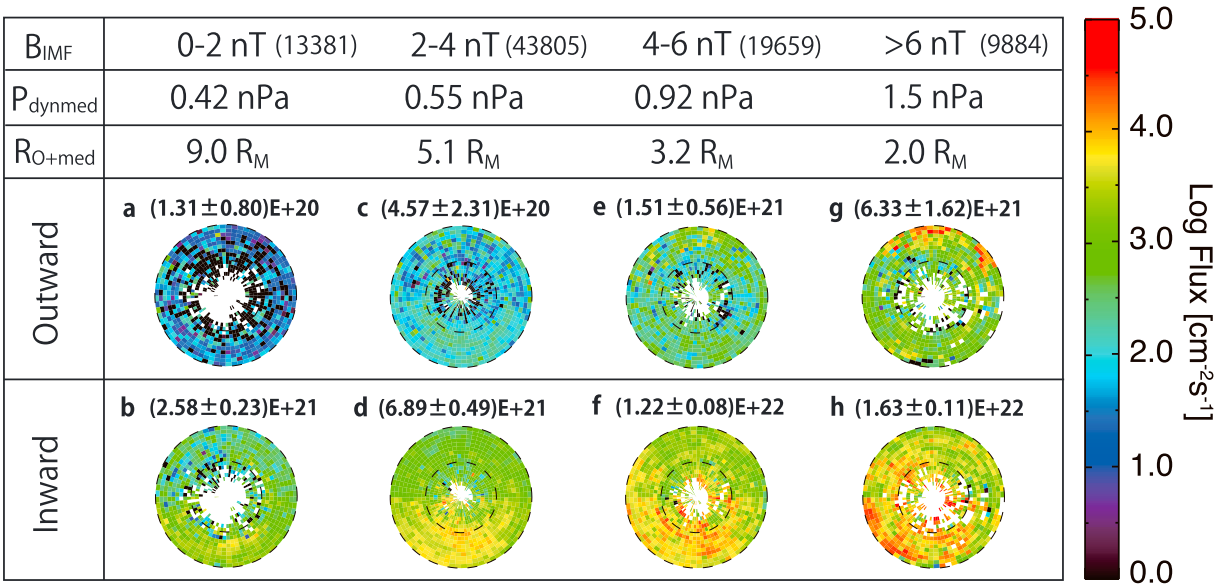

Figure 9. (a, c, e, and g) Outward and (b, d, f, and h) inward O^+ ion fluxes above the bow shock when the IMF magnitude is 0–2 nT (Figures 9a and 9b), 2–4 nT (Figures 9c and 9d), 4–6 nT (Figures 9e and 9f), and >6 nT (Figures 9g and 9h). Numbers shown by IMF magnitudes indicate the number of VDFs used to calculate the O^+ fluxes. In each IMF magnitude case, a median value of the dynamic pressure and the gyroradius of O^+ pickup ions in the solar wind are also shown. Outgoing/incoming ion rates (s^{-1}) are also shown above each map.

back to the solar wind when the gyroradius are enough small compared to the scale of MPR. This may also increase the reflection ratio of incident O^+ pickup ions. Since the reflection ratio depends on the dynamic pressure as strongly as the IMF magnitude that controls the O^+ reflection in the magnetosheath, it is possible that the O^+ reflection occurs as frequently in MPR as in the magnetosheath. Since *Masunaga et al.* [2016] examined O^+ ion reflection features only in the magnetosheath, it is important to identify the reflection features in MPR and compare their occurrence frequency between the magnetosheath and MPR.

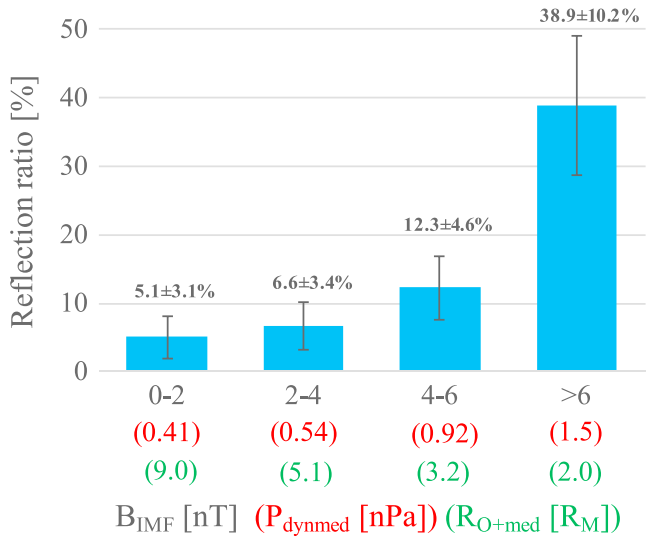

Figure 10. Reflection ratio of incident O^+ pickup ions for the four IMF magnitude cases. In each case, median values of the dynamic pressure and the gyroradius of O^+ pickup ions in the solar wind are also shown.

Figure 9 shows outward and inward O^+ ion fluxes as well as outgoing/incoming rates sorted into four IMF magnitude cases. In each case, we also calculated median values of the dynamic pressure and the gyroradius of O^+ pickup ions in the solar wind. We can see that the dynamic pressure positively correlates with the IMF magnitude, while the gyroradius negatively correlates with it. Although there are large lacks of data points in each map shown by white bins, we can see that both outward and inward fluxes clearly increase as the IMF magnitude and the dynamic pressure increase and as the O^+ gyroradius decreases. The resultant reflection ratios for the four cases are shown in Figure 10. We can see that the reflection ratio nonlinearly increases with the changes in

the IMF magnitude, the dynamic pressure, and the O^+ gyroradius. Especially, when these parameters are under extreme conditions ($B_{IMF} > 6$ nT and median values of P_{dyn} and R_{O+} are 1.5 nPa and 2.0 R_M, respectively), the reflection ratio increases to 38.9 ± 10.2%.

We have to note that although an error is large the largest reflection ratio was observed during the parallel IMF case as seen in Figure 4d. In this case, IMF nearly directs parallel to the solar wind flow, and thus, the O^+ gyroradius becomes small due to small V_{SWperp}. Since the reflection ratio becomes large for the small gyroradius case as discussed above, the reflection ratio for the small cone angle case may become also large. In addition, a wide parallel shock likely forms near the nose of the bow shock in the parallel IMF case. This results in forming the foreshock region upstream Mars. In the Martian foreshock, strong fluxes of O^+ ion beams outgoing from the bow shock are observed by *Yamauchi et al.* [2015] for which the acceleration mechanism is still uncertain. Thus, it is possible that the large reflection ratio in the parallel IMF case may be caused by the O^+ beams in the foreshock formed near the parallel shock. To confirm this, we need more detailed analysis of O^+ ion VDFs under the parallel IMF case and study effects of the parallel shock on the reflection of incident O^+ pickup ions in the future.

It is known that the incident O^+ pickup ions are a major source of sputtering with the Martian upper atmosphere that drives atmospheric heating and escape [*Luhmann and Kozyra*, 1991]. Our observation shows that the reflection ratio is sharply increased to 38.9 ± 10.2% when the IMF magnitude and dynamic pressure are very large and gyroradius of O^+ pickup ions in the solar wind is very small ($B_{IMF} > 6$ nT and median values of P_{dyn} and R_{O+} are 1.5 nPa and 2.0 R_M, respectively). This implies that under the extreme solar wind condition a significant amount of incident O^+ pickup ions do not reach the exobase, which could reduce the sputtering consequences. Since the sputtering escape is thought to be important at the ancient Mars when the Sun and solar wind were more active than they are today [*Luhmann et al.*, 1992], it is important to study the effect of the O^+ reflection on the sputtering escape. However, our study only includes incident O^+ pickup ions reentering from the solar wind across the bow shock but denser newborn pickup ions also exist below the bow shock [*Masunaga et al.*, 2016]. These ions may be a main source for the sputtering especially in the −E hemisphere although they are not highly accelerated compared with incident O^+ pickup ions entering from the solar wind. Thus, we need to take these ions into account to study the effect of the O^+ ion reflection on the sputtering escape at Mars in future works.

According to our observations, solar wind conditions more likely to affect the reflection ratio of incident O^+ pickup ions than the solar EUV condition and the crustal magnetic field at Mars. Since the solar EUV flux does not significantly change the reflection ratio but inward/outward fluxes, it only contributes to O^+ ion productions around Mars. We conclude that the effect of the solar EUV flux on the ion reflection is small. Although effects of the position of the southern crustal magnetic fields on the reflection ratio are weak in our result, this does not mean that the crustal magnetic field never affect the incident O^+ pickup ions. It is possible that the incident O^+ ions are reflected by the crustal magnetic field with the same analogy to the reflection occurred in the magnetosheath shown in *Masunaga et al.* [2016]. Because the reflection ratio is larger under strong IMF and magnetic fields below the bow shock shown in Figure 10 and the magnitude of the crustal magnetic field typically reaches several hundred nanoteslas, it is possible that O^+ ion reflections locally occur more frequently than those seen in the magnetosheath. Thus, we plan to analyze the ion VDFs and study the ion reflection near the crustal magnetic field in the future work.

5. Conclusion

It was recently found that some of incident O^+ pickup ions are reflected in the Martian magnetosheath and return to the solar wind as a beam with energy of ~10 keV or higher [*Masunaga et al.*, 2016]. In this paper, to evaluate the importance of the reflection of incident O^+ pickup ions, we statistically estimated a reflection ratio by calculating average inward and outward O^+ ion fluxes (>10 keV) above the Martian bow shock. Using ~1.3 year data set (November 2014 to February 2016) of O^+ ion velocity distribution functions obtained from the STATIC instrument on MAVEN, we obtained three main results:

1. An average reflection ratio is 14.1 ± 6.7%.

2. The reflection ratio depends mainly on the IMF magnitude, the solar wind dynamic pressure, and the gyroradius of O^+ pickup ions in the solar wind. The solar EUV flux and the crustal magnetic field do not significantly affect the reflection ratio.
3. The reflection ratio becomes large as the IMF magnitude and the dynamic pressure increase and as the O^+ gyroradius decreases. Under the extreme solar wind condition ($B_{IMF} > 6$ nT and median values of P_{dyn} and R_{O+} are 1.5 nPa and 2.0 R_M, respectively), the reflection ratio increases to 38.9 ± 10.2%.

From these results, we suggest that magnetic fields both in the solar wind and below the bow shock determine the reflection ratio of the incident O^+ pickup ions by controlling the gyroradius of O^+ pickup ions. Since the reflection ratio depends on the dynamic pressure as much as the IMF magnitude that controls the sheath magnetic field, it is possible that the O^+ ion reflection occurs in MPR as frequently as it does in the magnetosheath. Since incident O^+ pickup ions are known to be a major source of atmospheric sputtering escape from Mars, our result suggests that ion reflections may have a role to reduce the sputtering escape from Mars under the extreme solar wind condition.

The effect of the crustal magnetic field on the ion reflection seems to be weak at Mars. However, it is possible that incident O^+ ions are reflected locally near the crustal magnetic field because the magnitude of the crustal magnetic field typically reaches several hundred nanoteslas. Thus, it is important to study ion VDFs near the crustal magnetic field on Mars.

Acknowledgments
This work was supported by Grant-in-Aid for JSPS Fellows 14J03613. This work was also supported by the Program for Advancing Strategic International Networks to Accelerate the Circulation of Talented Researchers G2602 and Grant-in-Aid for Scientific Research (B) 15H0731. The MAVEN project is supported by NASA Mars Exploration Program. The MAVEN data are available in NASA Planetary Data System.

References

Barabash, S., and R. Lundin (1993), Reflected ions near Mars: Phobos-2 observations, *Geophys. Res. Lett.*, *20*(9), 787–790, doi:10.1029/93GL00834.

Brain, D. A., J. S. Halekas, R. Lillis, D. L. Mitchell, R. P. Lin, and D. H. Crider (2005), Variability of the altitude of the Martian sheath, *Geophys. Res. Lett.*, *32*, L18203, doi:10.1029/2005GL023126.

Coates, A., and G. A. Jones (2009), Plasma environment of Jupiter family comets, *Planet. Space Sci.*, *57*, 1175, doi:10.1016/j.pss.2009.04.009.

Connerney, J. E. P., J. Espley, P. Lawton, S. Murphy, J. Odom, R. Oliversen, and D. Sheppard (2015), The MAVEN magnetic field investigation, *Space Sci. Rev.*, doi:10.1007/s11214-015-0169-4.

Cravens, T. E., A. Hoppe, S. A. Ledvina, and S. McKenna-Lawlo (2002), Pickup ions near Mars associated with escaping oxygen atoms, *J. Geophys. Res.*, *107*(A8), 1170, doi:10.1029/2001JA000125.

Crider, D., D. Vignes, A. M. Krymskii, T. K. Breus, N. F. Ness, D. L. Mitchell, J. A. Slavin, and M. H. Acuña (2003), A proxy for determining solar wind dynamic pressure at Mars using Mars Global Surveyor data, *J. Geophys. Res.*, *108*(A12), 1461, doi:10.1029/2003JA009875.

Dong, Y., X. Fang, D. A. Brain, J. P. McFadden, J. S. Halekas, J. E. Connerney, S. M. Curry, Y. Harada, J. G. Luhmann, and B. M. Jakosky (2015), Strong plume fluxes at Mars as observed by MAVEN: An important planetary ion escape channel, *Geophys. Res. Lett.*, *42*, 8492–8950, doi:10.1002/2015GL065346.

Dubinin, E. M. F., J. Woch, S. Barabash, R. Lundin, and M. Yamauchi (2006), Hydrogen exosphere at Mars: Pickup protons and their acceleration at the bow shock, *Geophys. Res. Lett.*, *33*, L22103, doi:10.1029/2006GL027799.

Edberg, N. J. T., M. Lester, S. W. H. Cowley, and A. I. Eriksson (2008), Statistical analysis of the location of the magnetic pileup boundary and bow shock and influence of crustal magnetic field, *J. Geophys. Res.*, *113*, A08206, doi:10.1029/2008JA013096.

Eparvier, F. G., P. C. Chamberlin, T. N. Woods, and E. M. B. Thiemann (2015), The solar extreme ultraviolet monitor for MAVEN, *Space Sci. Rev.*, doi:10.1007/s11214-015-0195-2.

Fang, X., M. W. Liemohn, A. F. Nagy, Y. Ma, D. L. De Zeeuw, J. U. Kozyra, and T. H. Zurbuchen (2008), Pickup oxygen ion velocity space and spatial distribution around Mars, *J. Geophys. Res.*, *113*, A02210, doi:10.1029/2007JA012736.

Fang, X., S. W. Bougher, R. E. Johnson, J. G. Luhmann, Y. Ma, Y.-C. Wang, and M. W. Liemohn (2013), The importance of pickup oxygen ion precipitation to the Mars upper atmosphere under extreme solar wind conditions, *Geophys. Res. Lett.*, *40*, 1922–1927, doi:10.1002/grl.50415.

Halekas, J. S., E. R. Taylor, G. Dalton, G. Johnson, D. W. Curtis, J. P. McFadden, D. L. Mitchell, R. P. Lin, and B. M. Jakosky (2015), The Solar Wind Ion Analyzer for MAVEN, *Space Sci. Rev.*, *195*(1), 125–151, doi:10.1007/s11214-013-0029-z.

Hara, T., K. Seki, Y. Futaana, M. Yamauchi, S. Barabash, A. O. Fedorov, M. Yagi, and D. C. Delcourt (2013), Statistical properties of planetary heavy-ion precipitations toward the Martian ionosphere obtained from Mars Express, *J. Geophys. Res. Space Physics*, *118*, 5348–5357, doi:10.1002/jgra.50494.

Lammer, H., H. I. M. Lichtenegger, C. Kolb, I. Ribas, E. F. Guinan, R. Abart, and S. J. Bauer (2003), Loss of water from Mars: Implications for oxidation of the soil, *Icarus*, *165*, 9–25, doi:10.1016/S0019-1035(03)00170-2.

Leblanc, F., and R. E. Johnson (2001), Sputtering of the Martian atmosphere by solar wind pick-up ions, *Planet. Space Sci.*, *49*(6), 645, doi:10.1016/S0032-0633(01)00003-4.

Luhmann, J. G., and J. U. Kozyra (1991), Dayside pickup oxygen ion precipitation at Venus and Mars: Spatial distributions, energy deposition and consequences, *J. Geophys. Res.*, *96*(A4), 5457–5467, doi:10.1029/90JA01753.

Luhmann, J. G., R. E. Johnson, and M. H. G. Zhang (1992), Evolutionary impact of sputtering of the Martian atmosphere by O^+ pickup ions, *Geophys. Res. Lett.*, *19*(21), 2151–2154, doi:10.1029/92GL02485.

Luhmann, J. G., S. A. Ledvina, and C. T. Russell (2004), Induced magnetospheres, *Adv. Space Res.*, *33*, 1905, doi:10.1016/j.asr.2003.03.031.

Masunaga, K., K. Seki, D. A. Brain, X. Fang, Y. Dong, B. M. Jakosky, J. P. McFadden, J. S. Halekas, and J. E. P. Connerney (2016), O^+ ion beams reflected below the Martian bow shock: MAVEN observations, *J. Geophys. Res. Space Physics*, *121*, 3093–3107, doi:10.1002/2016JA022465.

McFadden, J. P., et al. (2015), MAVEN SuperThermal And Thermal Ion Composition (STATIC) instrument, *Space Sci. Rev.*, doi:10.1007/s11214-015-0175-6.

Mitchell, D. L., et al. (2016), The MAVEN Solar Wind Electron Analyzer, *Space Sci. Rev.*, doi:10.1007/s11214-015-0232-1.

Rahmati, A., D. E. Larson, T. E. Cravens, R. J. Lillis, P. A. Dunn, J. S. Halekas, J. E. Connerney, F. G. Eparvier, E. M. B. Thiemann, and B. M. Jakosky (2015), MAVEN insights into oxygen pickup ions at Mars, *Geophys. Res. Lett.*, *42*, 8870–8876, doi:10.1002/2015GL065262.

Rahmati, A., et al. (2017), MAVEN measured oxygen and hydrogen pickup ions: Probing the Martian exosphere and neutral escape, *J. Geophys. Res. Space Physics*, doi:10.1002/2016JA023371.

Ramstad, R., S. Barabash, Y. Futaana, H. Nilsson, X.-D. Wang, and M. Holmström (2015), The Martian atmospheric ion escape rate dependence on solar wind and solar EUV conditions: 1. Seven years of Mars Express observations, *J. Geophys. Res. Planets*, *120*, 1298–1309, doi:10.1002/2015JE004816.

Tatrallyay, M., C. T. Russell, J. G. Luhmann, A. Barnes, and J. D. Mihalov (1984), On the proper Mach number and ratio of specific heats for modeling the Venus bow shock, *J. Geophys. Res.*, *89*(A9), 7381–7392, doi:10.1029/JA089iA09p07381.

Wang, Y.-C., J. G. Luhmann, F. Leblanc, X. Fang, R. E. Johnson, Y. Ma, W.-H. Ip, and L. Li (2014), Modeling of the O^+ pickup ion sputtering efficiency dependence on solar wind conditions for the Martian atmosphere, *J. Geophys. Res. Planets*, *119*, 93–108, doi:10.1002/2013JE004413.

Wang, Y.-C., J. G. Luhmann, X. Fang, F. Leblanc, R. E. Johnson, Y. Ma, and W.-H. Ip (2015), Statistical studies on Mars atmospheric sputtering by precipitating pickup O^+: Preparation for the MAVEN mission, *J. Geophys. Res. Planets*, *120*, 34–50, doi:10.1002/2014JE004660.

Yamauchi, M., R. Lundin, R. A. Frahm, J.-A. Sauvaud, M. Holmström, and S. Barabash (2015), Oxygen foreshock of Mars, *Planet. Space Sci.*, *119*, 48–53, doi:10.1016/j.pss.2015.08.003i.